TECHNICAL ARTICLE

Effect of Sintering Temperature on Microstructure, Mechanical, and Tribological Behavior of Aluminum-Based Composites Containing Double-Layered Al/CuFe Core-Shell Particulates

Rashid Ali, Fahad Ali, Aqib Zahoor, Rub Nawaz Shahid, Naeem ul Haq Tariq, Muhammad Yasir, Saad Nazir, and Hasan Bin Awais

In this study, the effect of sintering temperature on microstructure, mechanical and tribological behavior of aluminum matrix composites (AMCs) reinforced with Al/CuFe double-layered core-shell particulates (DLCSP) was investigated. In the first step, galvanic replacement and electroless deposition methods were employed to synthesize DLCSP by depositing submicron layers of copper and iron on Al particles, respectively. In the next step, 20 vol. % of DLCSP were blended with Al powder followed by hot-pressing at 440 °C, 480 °C, and 520 °C to fabricate the AMCs. The distribution of reinforcement, microstructural changes and wear track morphology of the prepared AMCs were investigated using scanning electron microscopy (SEM) with built-in energy-dispersive spectroscopy (EDX) system. Moreover, the mechanical and tribological behavior of the composites was studied using hardness, compression strength, and coefficient of frictions (COF). The results indicated that an increase in sintering temperature results in improved hardness, compressive strength, and COF. Further, strength along with toughness was preserved in these specially tailored DLCSP-reinforced AMCs.

1. Introduction

Iron and copper both are plentiful elements on earth. In the earth's crust, iron is the fourth most abundant constituent after oxygen, silicon, and aluminum (Ref 1). Iron is vital for life due to its uncountable characteristics (Ref 2). Similarly, copper is the most commonly plated element on different substrates due to its anti-biofouling, electrical and thermal conductivity (Ref 3-7). The solubility of Cu in Fe near its melting point is ∼ 10 atomic %. However, below 500 °C, the solubility of the former is reduced to less than 0.2 %. Similarly, Fe solubility in Cu is ∼ 4 atomic % near its melting point which is reduced to ∼ 0.2 % at room temperature. These elements are almost immiscible at room temperature despite similar atomic radii due to the positive enthalpy of mixing (Ref 8, 9). Combining such elements with positive heat of mixing is always a challenging task for researchers. Solubility limit has been extended by the use of non-equilibrium processes and Cu-Fe-based engineering materials have been applied in various applications due to their catalytic effect, magnetic, mechanical, energy storage, thermal and electrical characteristics (Ref 10-17). Rapid solidification, atomization, levitation, powder metallurgy, laser beam surface treatment, electrodeposition, electroless deposition, magnetron sputtering, etc., are the possible non-equilibrium processing techniques to circumvent the restrictions of conventional processes (Ref 16, 17, 19-24). After the first experiment under microgravity in space, the synthesis of Cu/Fe core-shell or egg-type structure made it possible to combine such elements (Ref 18). Nowadays, in quest of new materials, egg-like or core-shell reinforcement (developed in situ in aluminum matrix composites (AMCs)) is being reported by various research groups (Ref 25-30). Although multilayered composite structures can be developed using different methods in bulk materials such as explosive welding (Ref 31-33), however, in this study, our focus is to utilize pre-synthesized core-shell particulate in AMCs.

At present, core-shell particulate-reinforced aluminum matrix composites (CS-PRAMCs), prepared via powder metallurgy (PM), are showing prevailing trends in the fabrication of composites. In AMCs, reinforced with pure metallic particles (Fe, Cu, Ti, Ni), uniform hard shells of intermetallic around the ductile metallic core are formed in situ during processing (Ref 25-30). In such composites, the cracks formed in the reinforcements are restrained within the intermetallic shell, and thus, the crack is smaller than the thickness of the shell (Ref 34-36). Such resistance to crack growth is not probable in conventional AMCs reinforced with ceramic particulates (Ref 37). Moreover, in core-shell particles-reinforced AMCs, both tips of such a

Rashid Ali, Fahad Ali, Aqib Zahoor, Rub Nawaz Shahid, Naeem ul Haq Tariq, and Hasan Bin Awais, Department of Metallurgy and Materials Engineering, Pakistan Institute of Engineering and Applied Sciences (PIEAS), Islamabad, Pakistan; Muhammad Yasir, Department of Materials Science and Engineering, Institute of Space and Technology (IST), Islamabad, Pakistan; and Saad Nazir, Mechanical and Nuclear Engineering Department, University of Sharjah, Sharjah, UAE. Contact e-mail: fahadali62@hotmail.com.

crack face ductile matrix and core. Therefore, crack propagation is expected to be delayed by blunting of the crack tips. The restricted or delayed propagation of this crack, during plastic deformation of composites, causes improvement in ductility. Moreover, a contiguous network of hard intermetallic phases can improve the mechanical, electrical and thermal behavior of composites. An irregular intermetallic shell works as a stress concentrator that damages the mechanical behavior of composites. Therefore, it is important to form a uniform hard shell around the ductile core to get a good combination of strength and ductility in the composites. However, uniform shell formation required a complex combination of heating and mechanical working (Ref 30). Though pre-synthesized single-layered particles (Al/Cu) have been reported (Ref 37), but multilayered particles can be beneficial to accommodate deformation by increasing crack path. In view of this knowledge, first-time pre-synthesized multilayered core-shell particulate reinforcements, having immiscible metals, are utilized as reinforcement in AMCs. This novel work aims to synthesize Al/CuFe double-layered core-shell powder (DLCSP) by galvanic replacement and electroless deposition processes. To authors' knowledge, pre-synthesized DLCSP reinforcements have been used for the first time to develop AMCs with tailored microstructure to achieve remarkable trade-off between the strength and the toughness. The pre-synthesized Al-CuFe DLCSP were further incorporated as reinforcement to produce aluminum-based composites with unique microstructure by hot pressing. To understand the effect of consolidation temperature on microstructure, densification, hardness, compressive and tribological behavior of the composites were investigated in detail.

2. Materials and Method

To synthesize Al/CuFe DLCSP, high purity (purity > 99.5%) spherical Al powder (D_{50}: 10 μm) was deposited with copper and iron, respectively. To synthesize DLCSP, surface pretreatment of Al powder was initially carried out. For this purpose, 5 ml of 33 % ammonia solution was mixed in 45 ml of distilled water to prepare the pretreatment (etching) solution. In this solution, 2.0 grams of Al particles were etched for 2.0 minutes. In the next steps, copper and iron deposition was carried out on pretreated Al particles. For this purpose, the slurry of surface-treated Al particles was directly poured into a copper deposition bath maintained at pH 9.0 at 55 °C for 15 minutes. Then, after filtering and washing, Al/Cu composite powder was again immersed in an iron deposition bath with pH 9.2 at 80 °C for 10 minutes. The detailed baths compositions are as follows:

Copper Bath: Copper sulfate ($CuSO_4 \cdot 5H_2O$) 0.10 mol.L^{-1} as the main salt, Ethylene diamine tetraacetic acid, disodium (EDTA-2Na. $2H_2O$) 0.20 mol.L^{-1} as a complexing agent, Copper chloride ($CuCl_2$) 0.005 mol.L^{-1}, Boric acid (H_3BO_3) 0.5 mol.L^{-1} as a buffer (Ref 38).

Iron Bath: Iron sulfate ($FeSO_4 \cdot 7H_2O$) 0.10 mol.L^{-1} as the main salt, Sodium potassium tartrate ($KNaC_4H_4O_6 \cdot 4H_2O$) 0.22 mol.L^{-1} as a complexing agent, Citric acid ($C_6H_8O_7$) 0.03 mol.L^{-1}, Sodium hypophosphite (NaH_2PO_2. H_2O) 0.40 mol.L^{-1} as reducing agent, Boric acid (H_3BO_3) 0.5 mol.L^{-1} as a buffer (Ref 39).

After deposition of successive layers of copper and iron, respectively, the composite powder was filtered and washed with hot distilled water and dried in an oven for 8 hours at 80 °C. The density measurement of Al/CuFe powder was carried out by a helium gas pycnometer. The density values were used to estimate the volume fraction (20 %) of pre-synthesized Al/CuFe reinforcement in the Al matrix. Al and Al/CuFe powder were blended with a powder mixer rotator (Glas Col) for 4 hours at 60 rpm in a glass jar. The resultant blend was uniaxially hot-pressed at 440 °C, 480 °C, and 520 °C. A thin film of boron nitride was sprayed after cleaning the die and punches to reduce the friction. Subsequently, the powder blend was poured into a die (ø 10 mm). After lowering the upper punch, the chamber was evacuated (1×10^{-3} Pa) followed by desired load application (640 MPa) for 20 minutes of compaction. Argon gas was continuously purged in the chamber (40×10^3 Pa) to maintain an inert environment during hot pressing.

From each hot-pressed cylinder (ø 10 mm and length 10 mm), three samples (ø 3 mm and length 6 mm) were machined by using electrode discharge machining (wire cut) for quasi-static compression tests (strain rate 10^{-4} s^{-1}) at the room. A part of the composite sample was used to investigate the wear behavior. The process flow of hot-pressing is shown in Fig. 1. Identification of phases in pre-synthesized powder and hot-pressed cylinders were carried out by x-ray diffraction (XRD) using Cu Kα radiation (0.154 nm) source. The influence of sintering temperature on microstructural changes (due to interfacial reactions at interfaces) was probed by Tescan MAIA3 field emission scanning electron microscope (FE-SEM) with an in-built energy-dispersive x-ray spectrometer (EDX). A series of eight consecutive Vickers hardness (at 0.3 Kg load for 15 sec) readings were taken to avoid any ambiguity in results for each composite.

Dry sliding wear tests on the hot-pressed disks (ø 10 mm) of composites were performed at room temperature using a ball-on-disk system. Initially, these disks were ground and polished up to 2000 grit papers and washed with alcohol. For wear tests, a hardened steel ball (ø 6 mm) was used as a counter material. For all wear tests, a normal load of 2.0 N, wear track diameter ø 6 mm, and counter material speed of 150 rpm were selected. The wear tests time was kept in correspondence with wear length (20 m). The sliding distance and friction coefficient were dynamically recorded in the computer program. Wear surface topography was analyzed by SEM.

3. Results and Discussion

3.1 Characterization of Al/CuFe powder

The morphology of aluminum particles, before and after deposition of simultaneous layers of copper and iron, is shown in Fig. 2(a, b). The initial smooth surface of aluminum particles becomes rough after the deposition of layers. Initially, most aluminum particle surfaces are covered by an adherent, dense and nano-grained copper layer. Applying Scherrer formula on the XRD line scan of Al/CuFe core-shell powder before consolidation indicates average crystallite size of Cu to be 180 nm. Moreover, in our previously published work (Ref 37), SEM micrograph shows grain size of Cu to be ∼ 200 nm in core-shell particles. These results clearly confirm the existence
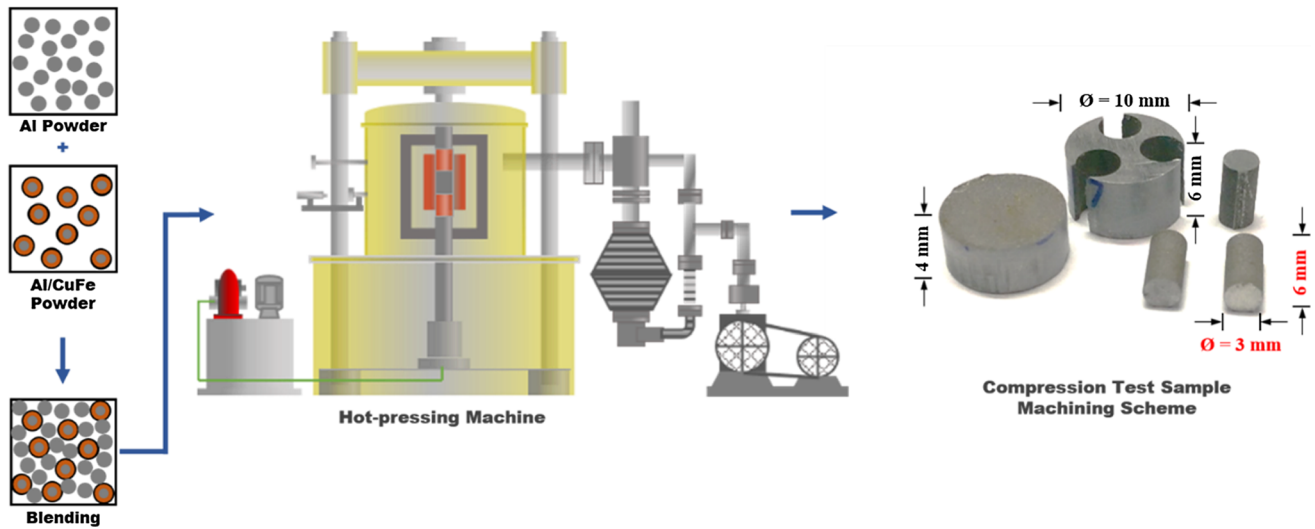
Fig. 1 The process flow of hot-pressing and machining scheme of tests sample
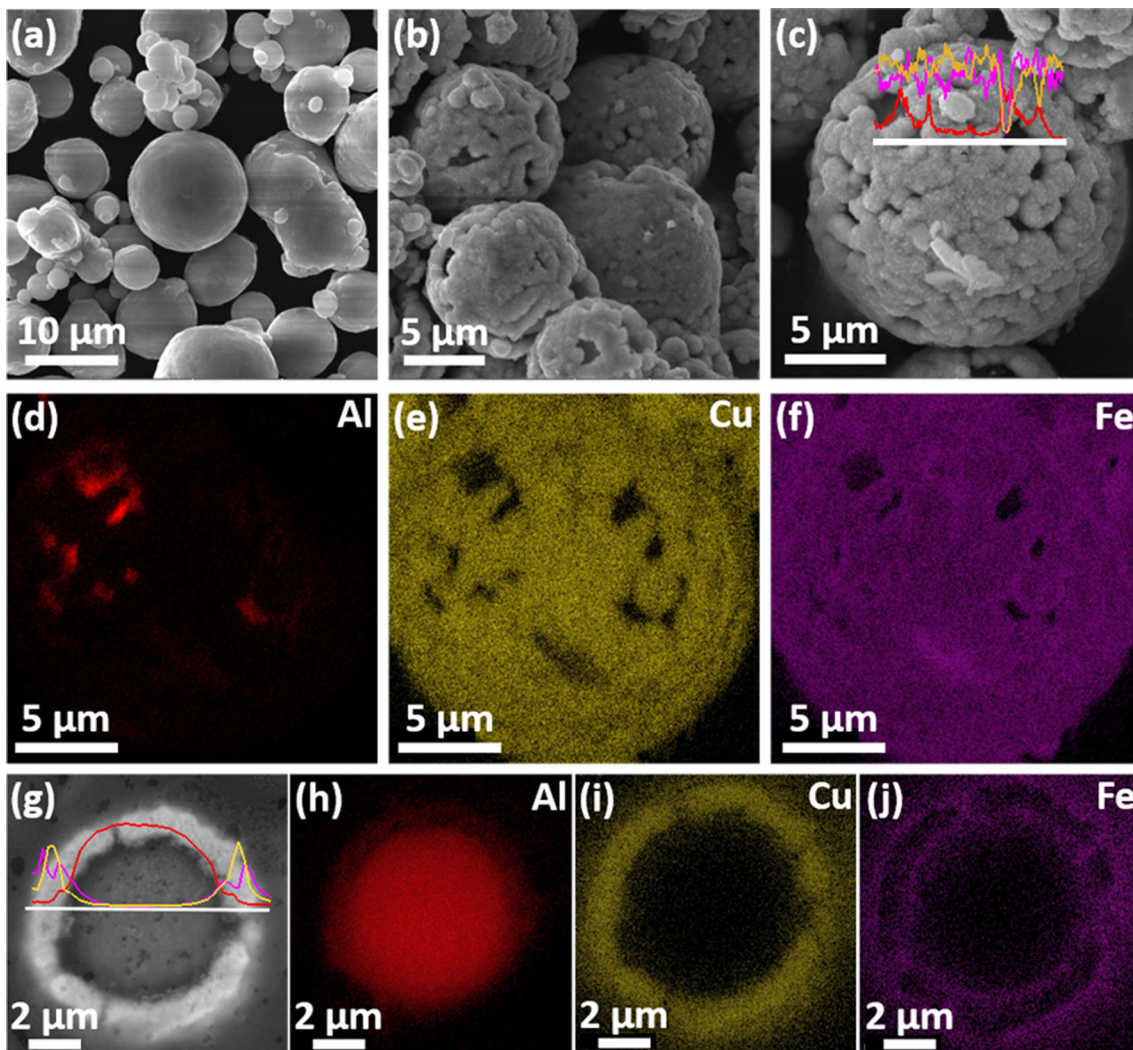

Fig. 2 SEM micrograph of (a) aluminum powder, (b) Al/CuFe composite powder, Al/CuFe powder particle with EDX line scan (c) and surface mapping (d, e, f), Similarly cross-sectional view of A/CuFe powder particle with (g) EDX line scan and (h, i, j) surface mapping

of nano-grained copper layer in reinforcement particles before consolidation. During the secondary shell formation, iron layer covers up Al/Cu composite powder particles. The effect of different chemical and process parameters for the deposition of these layers has been discussed in our previous work (Ref 38, 39). Results suggest that during the copper layer formation on aluminum particles, thermodynamics and kinetics of deposition process are mainly dependent upon molar ratio of complexing agent/copper containing salt and bath temperature. Further, complexing agent is needed in excess as compared to metal salt in order to promote the deposition reaction. Moreover, a stable pH of 8.8 is needed for efficient Cu deposition. However, variation in the pH does not greatly affect the deposition process. On the other hand, pH and complexing agent concentration have been found to be the most important factors affecting the deposition rate of iron. Results show that bath temperature has much less significance in iron deposition as compared to copper deposition.

The EDX line scanning (Fig. 2(c)) and surface mapping (Fig. 2d-f) of single-particle and its cross section (Fig. 2g-J) correspond well to thin layers of copper and iron deposited on aluminum particle surface. The outer iron layer, one of two visible iron layers in Fig. 2(j), is associated with the iron directly deposited on the pre-deposited copper layer, whereas the inner ring is formed due to the direct reduction in iron ions on aluminum substrate. Fig. 3(a, b) shows higher magnification SEM micrograph of particle surface morphology after deposition. It can be observed that initially, the copper deposit has cauliflower-like morphology (Fig. 3a) which transforms to a granular surface (Fig. 3b) after iron deposition. For the deposition of iron on a copper substrate, it is well established that the aluminum surface should be in contact with copper (Ref 40). Further, Al works as a sacrificial element during the iron deposition on the copper layer. In the current scenario, during deposition of Fe on Al/Cu particles, Al (in the core) also acts as a sacrificial element. This phenomenon is evident from the delamination or dissolution of aluminum in particles (Fig. 3c). The aluminum dissolution rate was reduced by inserting pre-etched aluminum strips (02 Nos. with dimensions 25×25 mm^2) in the iron deposition bath. These strips provide extra contact area to enhance iron plating to avoid or slow down the dissolution/delamination of Al core. Moreover, as these particles were to be compacted during hot-pressing, therefore, Al delamination was not considered detrimental in achieving consolidation. The EDX results only show the

presence of elemental Al, Cu, and Fe phases in the prepared DLCS powder (Fig. 2).

The XRD patterns of synthesized powders, after deposition of Cu and CuFe layers, are shown in Fig. 4(a). The characteristic peaks of Cu and Al appear at different 2θ angles and are easily distinguished using JCPDF cards. However, peaks of Al and Fe at 44.8° and 65.1° appear at the same angles and could not be differentiated under given XRD scanning parameters. However, continuous decline in the height of Al peak at 2θ value of 38.6° indicates successive deposition of Cu and Fe layers. Thus, visible characteristic peaks of crystalline Cu, Fe, and Al from synthesized composite powders confirm the successful deposition of Cu and Fe layers on Al particles. The synthesized Al/Cu and Al/CuFe powders have single and multiple shells of Cu and CuFe, respectively, on Al particles. This is in agreement with EDX results, which only show the presence of Cu, Fe, and Al elements in the prepared particles (Fig. 2).

3.2 Effect of Sintering Temperature on

3.2.1 Microstructure of composite. Fig. 5 presents secondary electron SEM micrographs of the prepared AMCs, reinforced with 20 vol. % pre-synthesized Al/CuFe DLCSP, hot-pressed at 440 °C, 480 °C, and 520 °C for 20 minutes. The distribution and formation of agglomerates of reinforcing particles are evident from these micrographs. These agglomerates might have developed during the blending process. The color contrast of images in Fig. 5(a-f) indicates the chemical contrast i.e., brighter phase represents the CuFe and CuFe rich phases, while darker areas represent Al in matrix and core. It was anticipated that there should be a multilayered structure due to interfacial reactions between matrix and reinforcement to transform into intermetallic, as depicted in XRD. However, the expected multilayers are not visible in higher magnification SEM micrographs (Fig. 5 (b, d, and f)). The microstructural analysis shows that in all composites, the Al/CuFe reinforcing particles are well embedded in the Al matrix. Further, good bonding between Al-Al/CuFe interfaces (white arrows) is observed in all composites hot-pressed at 440 °C, 480 °C, and 520 °C. In contrast, the interfaces between reinforcing particles (Al/CuFe-Al/CuFe) in agglomerates were either not well bonded or partially bonded (yellow arrows) at 440 °C and 480 °C sintering temperature, respectively. The most probable reason for this lack of bonding may be associated with the iron
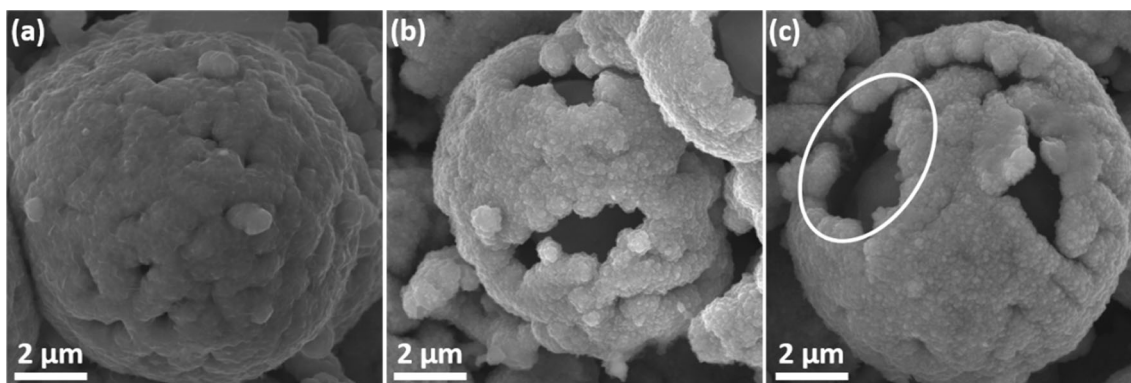
Fig. 3 SEM images showing morphology of deposited (a) copper, (b) iron layers. Panel (c) shows delamination of Al particle (encircled) from the deposited layers
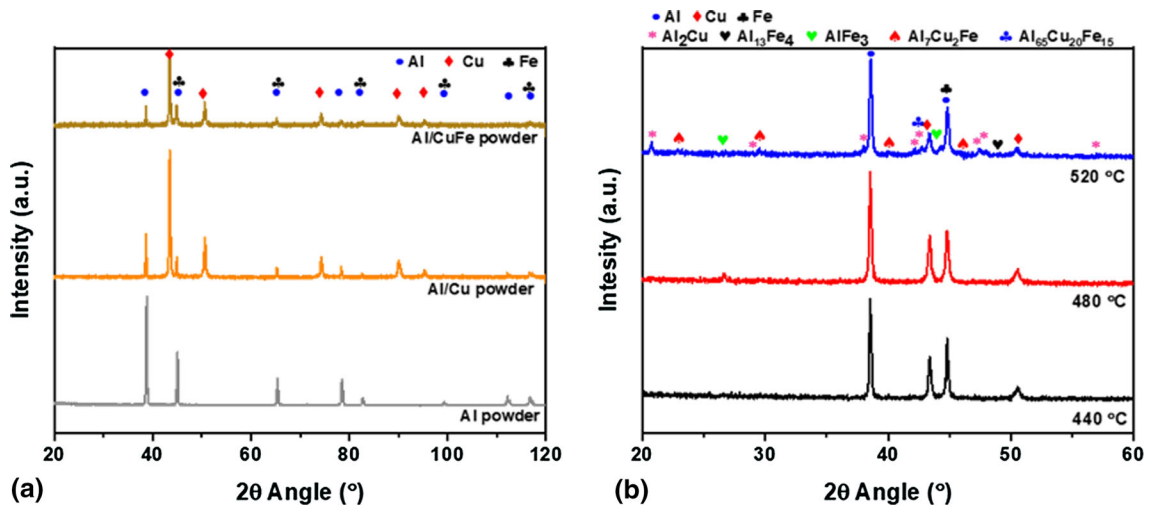
Fig. 4 XRD analysis of (a) pre-synthesized Al/CuFe core-shell powder (b) hot-pressed composites at 440 °C, 480 °C and 520 °C
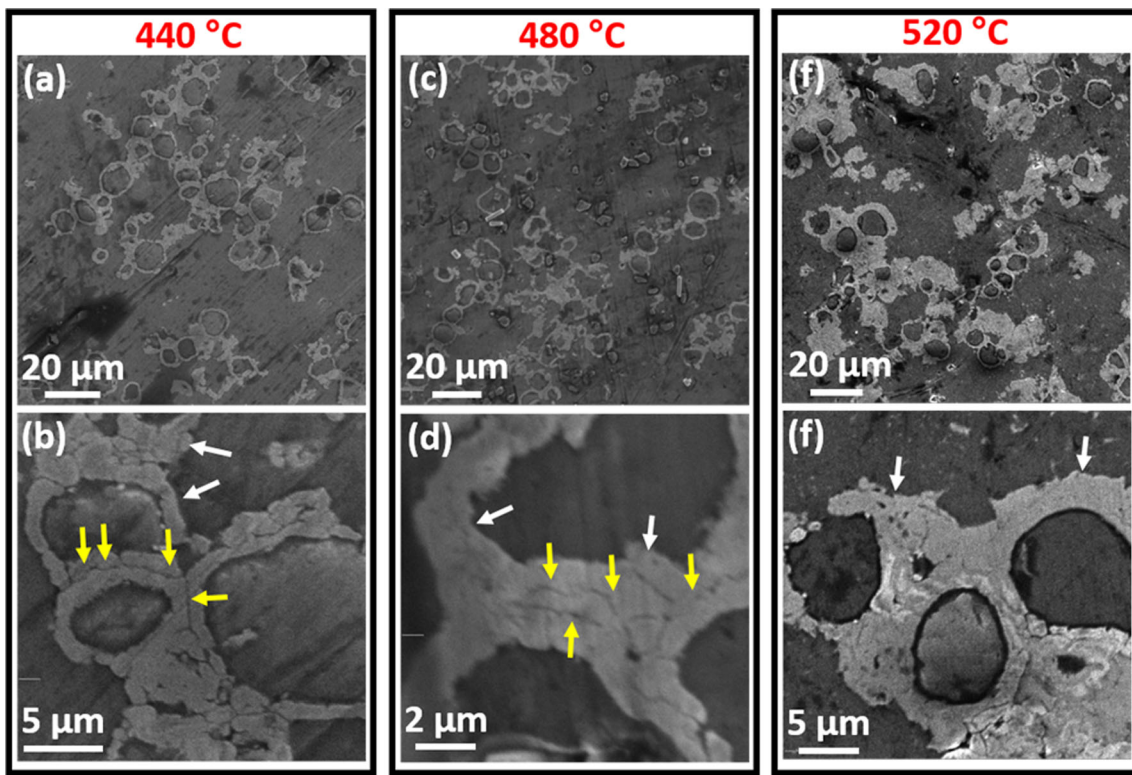
Fig. 5 SEM micrographs of hot-pressed composites at (a) 440 °C, (c) 480 °C, and (e) 520 °C, along with corresponding higher magnification micrographs (b), (d), and (f), respectively

layers present on the outer side of agglomerated reinforcing particles. These iron layers have low diffusivity at 440 °C and 480 °C. While, by increasing sintering temperature in the composite (hot-pressed at 520 °C), all interfaces have been properly amalgamated due to higher diffusional rates of the constituents. Moreover, an increase in thickness of the deposited layer, due to volumetric changes associated with interfacial reactions, is observed with increasing processing temperature. Additionally, the EDX of hot-pressed composite (520 °C) at higher magnification was performed (Fig. 6) which represents that Cu and Fe (double ring) remain intact after hot-pressing.

3.2.2 Phase Composition of Composite. For the phase's composition, the XRD analysis of all the prepared AMCs was performed (Fig. 4b). According to binary phase diagrams of AlFe and AlCu, five stable intermetallic phases in AlFe and five in the AlCu system are possible in solid diffusion couples. Cu and Al have relatively higher diffusivity coefficients as compared to that of Fe. Considering this, researchers have found that Al-Cu-based intermetallic phases are formed at relatively lower temperatures in comparison to Al-Fe-based aluminides. Previous studies on Al-Cu diffusion couples (Ref
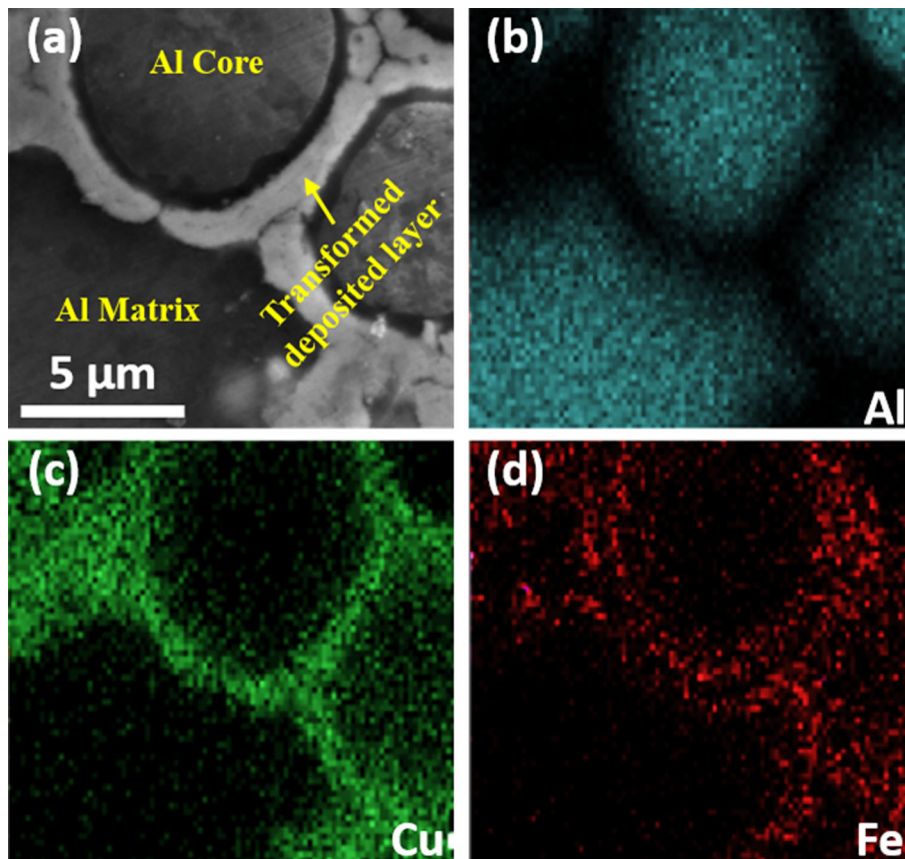
Fig. 6 SEM/EDX micrographs of (a) hot-pressed composites (520 °C) at higher magnification. Panel (b), (c), and (d) are EDX mapping for Al, Cu, and Fe, respectively

41) showed that atomic diffusion results in the evolution of Al_2Cu and Al_9Cu_4 phases due to low formation energy (Ref 42). Similarly, in the Al-Fe couple, the formation of $AlFe_3$ has been reported at a relatively lower temperature which transforms into other thermally stable intermetallic phases with further atomic diffusion. It has been reported that in ternary diffusion systems (involving Al, Cu and Fe as thin films), Al-Cu-based intermetallic phases always initially form upon heating without considering the stacking sequence of films. Upon further heating, the formation of Fe-based aluminides takes place. Cu and Fe-based aluminides interact to form ternary intermetallic ω-phase (Al_7Cu_2Fe) (Ref 43). Additionally, in AMCs reinforced with Al-Cu-Fe-based quasicrystals, the formation of ω-phase has also been reported at temperatures $\geq$ 450°C (Ref 44). In the current study, Al_2Cu has been observed after consolidation at 440°C (peak at 2θ value ∼47°), while formation of ω-phase and Fe-based aluminides have been observed at higher consolidation temperatures in accordance with previous studies.

Generally, thermodynamics and diffusion kinetics are responsible for the formation of intermetallic. Moreover, the formation of ternary phases (Al_7Cu_2Fe, $Al_{65}Cu_{20}Fe_{15}$) has been reported in the Al-Cu-Fe system during sintering (Ref 45). The XRD patterns in Fig. 4(b) show that there are five intermetallic phases (Al_2Cu, $AlFe_3$, Al_7Cu_2Fe, $Al_{65}Cu_{20}Fe_{15}$, $Al_{13}Fe_4$) are formed in the composites other than basic constituents. Among these intermetallic phases, only two phases (Al_2Cu and Al_7Cu_2Fe) are prominent. Moreover, as the processing temperature increases from 440 °C to 520 °C, the peak intensities of

intermetallic phases increase due to a higher degree of interfacial reaction except for the $AlFe_3$ phase. The XRD scan of the sample, sintered at 480 °C, has higher peak intensity which is associated with the $AlFe_3$ phase (at 2θ value 26.6°) when compared to the composites sintered at 440 °C and 520 °C. This indicates that the processing conditions of composite, consolidated at 480 °C, promote the formation of the $AlFe_3$ phase. Moreover, the visible XRD peak at 2θ values 43.4° and 50.3° relates to Cu presents that the Cu deposited layer was not transformed during the consolidation of composites. However, the Cu peak heights are continuously decreasing, which is an indication of a higher fraction of transformation of Cu with increasing consolidation temperature.

3.3 Physical and Mechanical Properties

Figure 7(a) illustrates the variation in density of the composites with increasing the sintering temperature from 440 °C to 520 °C. The oxide layer on Al or Cu-Fe surfaces may degrade the sintering ability of the elements. In general, higher temperatures facilitate the diffusion of elements to improve sintering ability which results in a decrease in porosities or pores between particles. But, in the present work, relative density (densification) varies from 99.92 % to 99.79 % with increasing temperature from 440 °C to 520 °C. The possible reasons behind the reduction in relative density while increasing temperature from 440 °C to 480 °C are: (1) volumetric adjustments due to the formation of aluminides (for example, $AlFe_3$ has higher molar volume) of deposited metals, (2) reduced compressibility due to higher fraction of intermetallic

phases formation and (3) differences in diffusion coefficients of constituents in composite (Kirkendall's effect) (Ref 46).

To assess the mechanical behavior of the prepared composites, a series of hardness and compression tests were performed. In hardness testing, eight readings were taken for each sample to avoid any ambiguity and average results are reported in Fig. 7(b). This figure illustrates the effect of sintering temperature on the Vickers hardness of the fabricated composites. As the sintering temperature is increased from 440 °C to 520 °C, a significant improvement in hardness, from 47.4 to 85.9 $HV_{0.3}$, is observed. The higher consolidation temperature leads to extensive interfacial reactions, resulting in a higher volume fraction of harder intermetallic phases in the composites. This is quite evident from peaks heights of respective intermetallic phases in XRD patterns shown in Fig. 4(b). These harder phases improve the overall hardness of the DLCSP-reinforced composites.

The engineering stress–strain curves of different hot-pressed AMCs are shown in Fig. 8(a) and corresponding properties are summarized in Fig. 8(b). By increasing the sintering temperature of AMCs from 440 °C to 520 °C, the ultimate compressive strength increases from 259 MPa to 387 MPa, while the fracture strain decreases from 41.3 % to 26 %. The improvement in compressive strength of the composites with increasing processing temperature can be attributed to 1) increased load-bearing capacity of the structure due to intermetallic formation (2) possible formation of dislocations in deposited shells of reinforcing particles due to in situ interfacial reactions between matrix and reinforcements. With the extent of interfacial reaction, the volume fraction of intermetallic and dislocation density at the interfaces is enhanced (Ref 47). The degree of in situ interfacial reactions with increasing temperature can be estimated from the thickness of the deposited layer after sintering (Fig. 4). Furthermore, the evolution of the thick and hard intermetallic layer is responsible for a decrease in fracture strain of the hot-pressed AMCs with increasing temperature from 440 °C to 520 °C.

The reduction in ductility with intermetallic phase evolution can be attributed to the increase in the number of pores at interfaces (Kirkendall's effect). These pores limit the stress transfer from matrix to reinforcements and result in reduced ductility. Moreover, pores act as stress risers to generate cracks during deformation and prohibit the dislocation gliding at the interfaces, thereby reducing the ductility. However, composites containing Al-Cu-Fe-based intermetallic reinforcements, without multi-shell structure processed with similar conditions (Ref 48), showed lower fracture strain as compared to the composites prepared in this study. The reason behind the higher
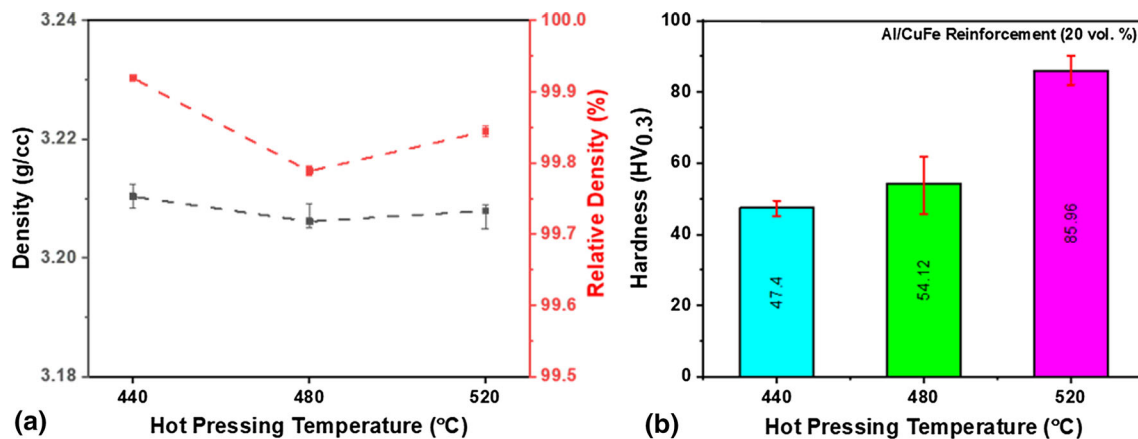
Fig. 7 Effect of sintering temperature on (a) density vs relative density (densification) and (b) Vickers hardness
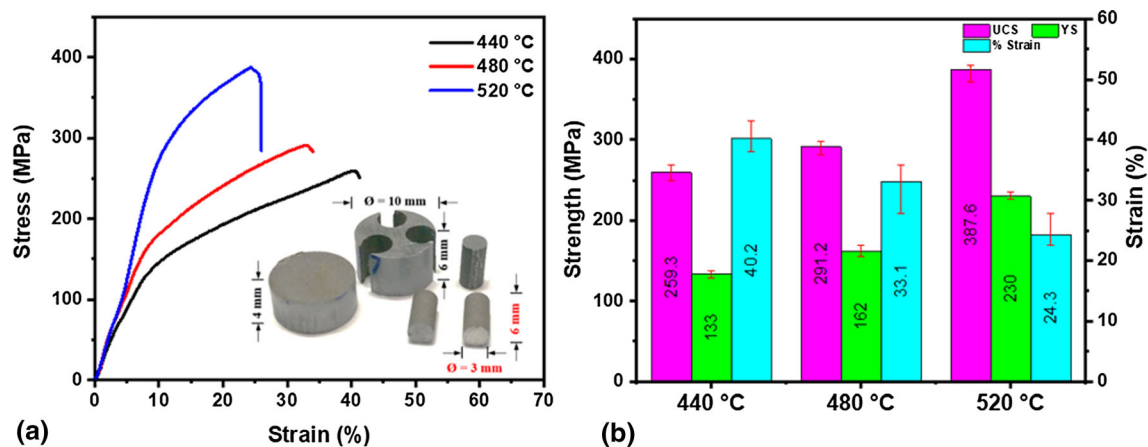
Fig. 8 Compressive stress–strain curve of AMCs hot-pressed at 440 °C, 480 °C and 520 °C (a) and summary of corresponding mechanical properties (b)
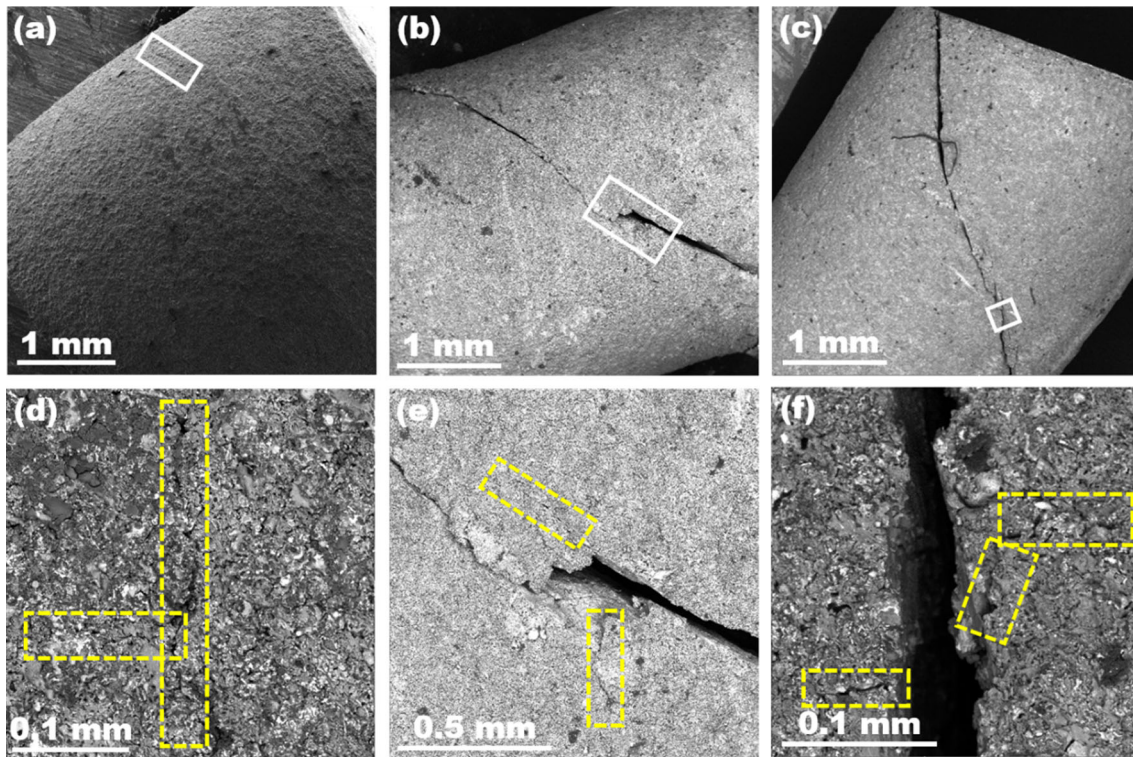
Fig. 9 SEM micrographs of composites hot-pressed at (a) 440 °C, (b) 480 °C, (c) 520 °C along with corresponding higher magnification images (d, e, f) of white rectangular areas marked in panels (a, b, c), respectively

fracture strain in the current study is associated with the multilayered core-shell structure of the reinforcing particles. The core-shell structure is reported to be responsible for increasing the crack path length (Ref 25, 31). Additionally, unreacted ductile Cu in shells provides extra resistance to crack propagation.

Furthermore, the lateral side of the fractured samples in compression testing was analyzed using SEM. The BSE-SEM micrographs (Fig. 9) show that with increasing consolidation temperature, the width of the major shear band increases. In the sample hot-pressed at 440 °C, the shear crack is not prominent due to the presence of unconsumed ductile Cu and Fe phases. Therefore, these ductile phases accommodate large strain as observed in the compression test result. However, at certain stress levels, small cracks appear in the sample. Due to these cracks, load-bearing capability decreases drastically. While, in other composites (hot-pressed at 480 and 520 °C) containing a higher volume fraction of intermetallic phases, branched and parallel shear cracks are visible along the main shear crack. Such cracks indicate the absorption of fracture energy to improve fracture toughness.

For further investigation, the BSE-SEM micrographs of the fractured surface of composites, consolidated at 480 and 520 °C, are shown in Fig. 10. The micrographs show presence of shear bands in the matrix as well as in core areas of reinforcing particles in both composites. These shear bands are responsible for absorbing strain energy during compression loading. Similarly, elongation of reinforcing particles can be noticed due to compressive stresses. Moreover, the delamination of shells from the Al-core can be observed for the composite hot-pressed at 520 °C as indicated by red arrows in Fig 10(b). This delamination can be attributed to higher degree of interfacial

transformation of Cu and Fe into harder intermetallic phases. These harder phases result in less deformation as compared to Al in the core areas. This abnormality at interfaces (with difference in elastic moduli) results in crack generation at the interfaces and (ii) crack arresting in core areas to accommodate the deformation.

3.4 Strengthening Mechanisms

The study of strengthening mechanisms in particulates-reinforced composites is important for materials scientists to understand the effect of microstructural features on mechanical behavior. To date, among numerous strengthening models, modified shear lag (MSL) theory is most suitable because of its reasonably accurate prediction of yield strength. The model deals with direct and indirect strengthening mechanisms. The direct strengthening includes load transfer mechanism 'f_l', while the indirect strengthening comprises (a) dislocation strengthening 'f_d' (Orowan strengthening (OR), geometric necessary dislocations (GND), thermal mismatch strengthening (TMS)) and (b) strengthening due to change in ligament size (λ) 'f_s'. The established MSL model, based on considering these three mechanisms ('f_l', 'f_d' and 'f_s'), has been expressed by the following equation (Ref 49, 50);

$$\sigma_y = \sigma_y^{\circ}(1+f_l)(1+f_d)(1+f_s)$$

The strengthening contribution by each mechanism was estimated according to the mathematical model. The results are given in Table 1. The factors f_l and f_s depend on the extent of interfacial reaction. As discussed earlier (section 3.2.1) the intermetallic phase formation due to interfacial reaction is enhanced with increasing sintering temperature. As a result, the
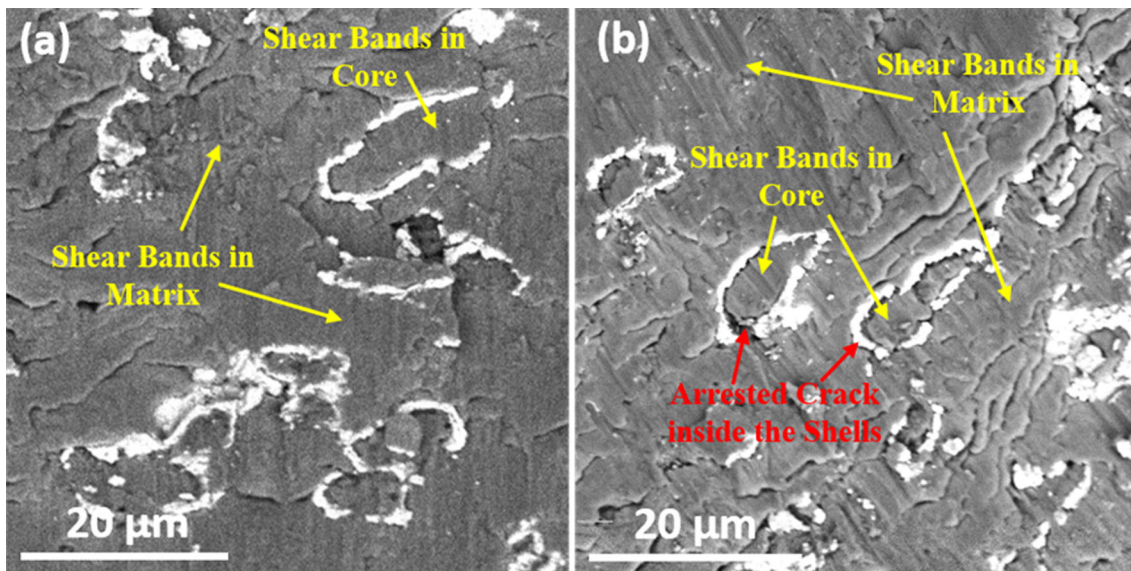
Fig. 10 SEM micrographs of fractured surfaces of composites hot-pressed at (a) 480 °C, and (b) 520 °C

Table 1 Calculated strengthening factors for composites

Sintering Temperature, °C	f_l	f_d	f_s
440	0.077	0.102	0.072
480	0.083	0.102	0.097
520	0.128	0.122	0.207

effect of load-bearing capacity and average matrix ligament size 'λ' increases with increasing sintering temperature. The factor f_d, on the other hand, is based on different strengthening mechanisms like Orowan strengthening, thermal mismatch strengthening, geometric necessary dislocations strengthening, etc., and is dependent upon multiple microstructural characteristics including the extent of interfacial reaction and distribution of reinforcements in the matrix.

3.5 Wear Behavior of Composites

Figure 11 presents the variation in coefficient of friction (COF) with increasing sliding distance of hot-pressed composites at different temperatures. Generally, in wear tests, there are some fluctuations in COF which tend to stabilize after certain sliding cycles/distance. Similar trends are observed in the present study; however, COF stabilization distances are different for all composites. The stabilization cycles for composites hot-pressed at 440 °C and 480 °C are 400 cycles (at sliding distance of 7.55 m), while COF tends to stabilize after 200 sliding cycles (at sliding distance of 3.77 m) for samples processed at 520 °C. Moreover, it was observed that the friction coefficient is around 0.4 for all hot-pressed composites. The results show that the friction coefficient for composite hot-pressed at 520 °C is more steady during the whole experiment while the composite hot-pressed at 440 °C shows the highest fluctuation in COF (as shown in Fig. 11) against the counter steel ball due to the large contact area between steel ball and wear track, which consequence in higher frictional force. The SEM micrographs of the wear tracks, shown in Fig. 12 (a-f),
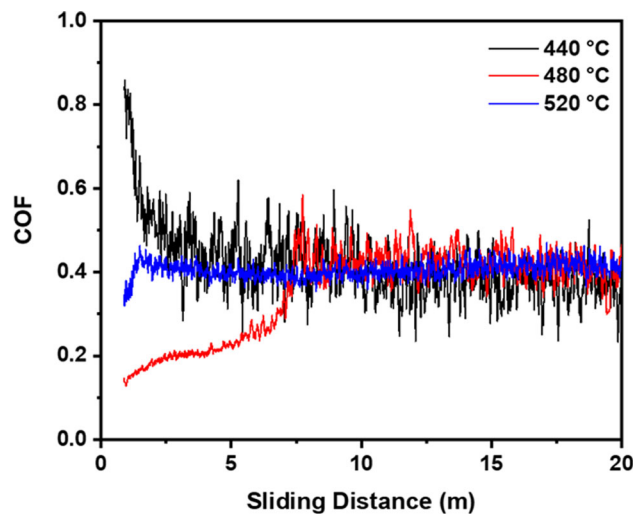
Fig. 11 Variation in coefficient of friction (COF) with increasing sliding distance of composites hot-pressed at different temperatures (440 °C, 480 °C, and 520 °C)

present a continuous improvement in wear resistance with increasing sintering temperature. As discussed above, the formation of intermetallic phases increases with increasing sintering temperature (Fig. 4(b)). The in situ formation of these hard intermetallic phases results in higher wear resistance. The composites hot-pressed at 440 °C and 480 °C (Fig. 12d and e, respectively) were predominantly worn out through delamination and adhesive wear mechanisms while the sample hot-pressed at 520 °C exhibited excellent wear performance showing sporadic abrasive wear marks (Fig. 12(f)). Further, a colony of worn intermetallic particles can be seen in Fig. 12(f). This is in line with the results presented in Fig. 4 wherein the peak intensities of intermetallic phases increase due to a higher degree of interfacial reaction.
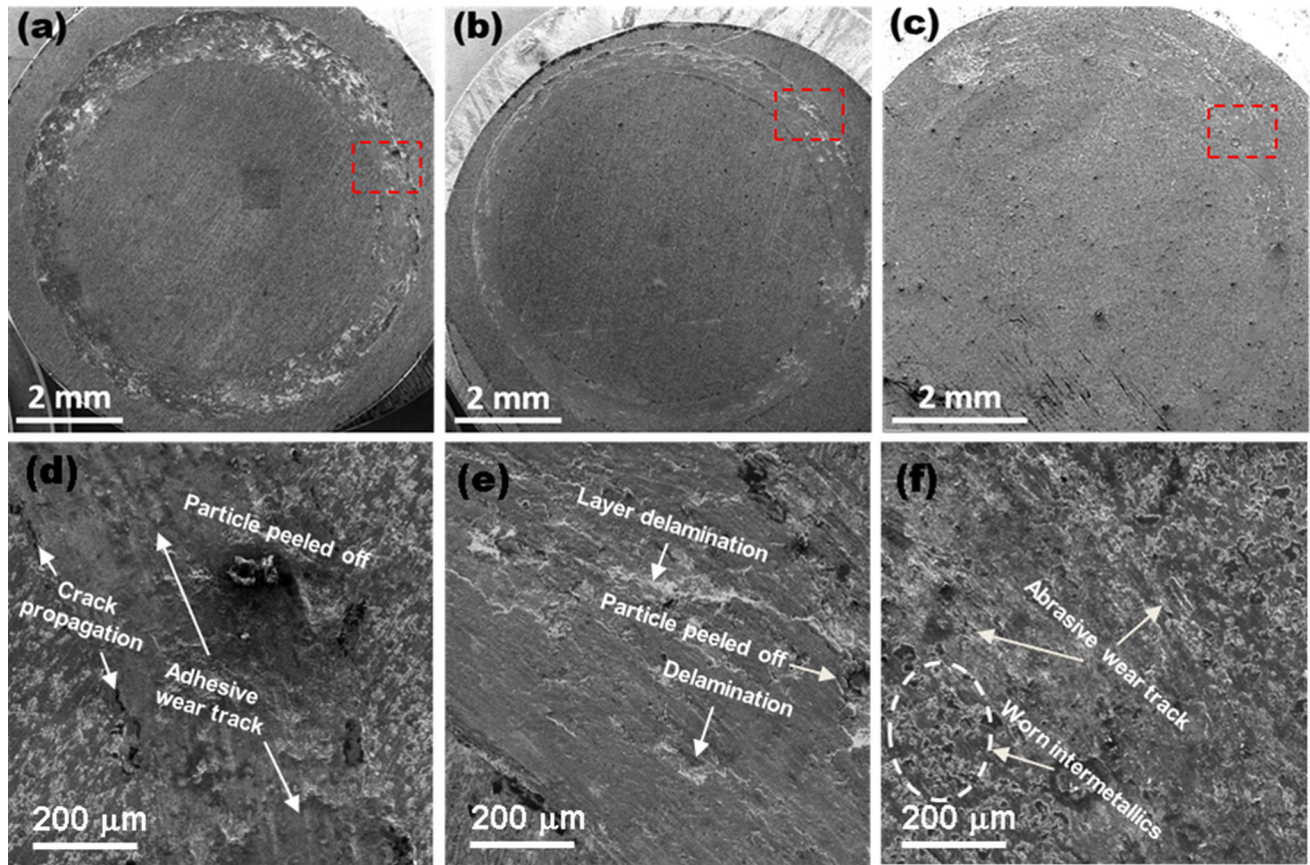
Fig. 12 The variation in wear tracks due to change in sintering temperatures (a) 440 °C, (b) 480 °C, and (c) 520 °C of composites. Panel (d), (e), and (f) shows high magnification image of SEM image of selected regions in panel (a), (b), and (c), respectively

4. Conclusions

In the current work, the effect of hot-pressing temperature on microstructure, mechanical and tribological behavior of aluminum matrix composites reinforced with pre-synthesized Al/CuFe DLCSP was investigated. The layers of copper and iron were deposited by galvanic replacement and electroless deposition methods on Al particles. The blend of these particles with Al powder was hot-pressed at 440 °C, 480 °C, and 520 °C to fabricate the AMCs. The key concluding points are as follows:

- The relative density of composites decreases with increasing temperature due to the formation of the hard intermetallic network which results in reduced compressibility of the composite powder compact.
- High temperature facilitates interfacial diffusion, which results in the transformation of deposited layers into hard intermetallic. These intermetallic phases increase the hardness and strength of fabricated composites with increasing temperature up to 86 $HV_{0.3}$ and 388 MPa. However, a 37 % decrease in ductility was observed during compression testing.
- The tribology of the composites indicates that increasing consolidation temperature from 440 to 520 °C results in a significant decrease in wear damage.
- It is anticipated that the findings of this work would facili-

tate the development of advanced engineering materials with an unprecedented combination of strength and toughness in transport, electrical packaging, chemical and aerospace industries.

References

1. A.A. Yaroshevsky, Abundances of Chemical Elements in the Earth's Crust, *Geochemistry Int.*, 2006, **44**, p 48–55.
2. N.C. Andrews, Forging a Field: The Golden Age of Iron Biology, *Blood*, 2008, **112**, p 219–230.
3. O.P. Abioye, C.A. Loto and O.S.I. Fayomi, Evaluation of Anti-biofouling Progresses in Marine Application, *J. Bio- Tribo-Corrosion*, 2019, **5**, p 1–8.
4. B.C. Sousa, C.J. Massar, M.A. Gleason and D.L. Cote, On the Emergence of Antibacterial and Antiviral Copper Cold Spray Coatings, *J. Biol. Eng.*, 2021, **15**, p 1–15.
5. Y. Pan, X. He, S. Ren, M. Wu and X. Qu, High Thermal Conductivity of Diamond/Copper Composites Produced with Cu–ZrC Double-Layer Coated Diamond Particles, *J. Mater. Sci.*, 2018, **53**, p 8978–8988.
6. I.B. Gomes, M. Simões and L.C. Simões, Copper Surfaces in Biofilm Control, *Nanomaterials*, 2020, **10**, p 2491.
7. P. Chen, H. Li, S. Hu, T. Zhou, Y. Yan and W. Pan, Copper-Coated TiN Nanofibers with High Electrical Conductivity: a New Advance in Conductive One-Dimensional Nanostructures, *J. Mater. Chem. C*, 2015, **3**, p 7272–7276.
8. S.C. Liu et al., A Surface Energy Driven Dissolution Model for Immiscible Cu-Fe Alloy, *J. Mol. Liq.*, 2018, **261**, p 232–238.

9. S.K. Sahu and A. Navrotsky, Thermodynamics of Copper-Manganese and Copper-Iron Spinel Solid Solutions, *J. Am. Ceram. Soc.*, 2017, **100**, p 3684–3692.

10. B. Ma, J. Li, Z. Xu and Z. Peng, Fe-shell/Cu-Core Encapsulated Metallic Phase Change Materials Prepared by Aerodynamic Levitation Method, *Appl. Energy*, 2014, **132**, p 568–574.

11. S.F. Zhou, J.B. Lei, Z. Xiong, J.B. Guo, Z.J. Gu and H.B. Pan, Effect of Fe Content on Microstructure and Mechanical Properties of Cu–Fe-Based Composite Coatings by Laser Induction Hybrid Rapid Cladding, *Trans. Nonferrous Met. Soc. China*, 2016, **26**(12), p 3196–3204.

12. K. Uenishi, Y. Ogata, S. Iwatani, A. Adachi, T. Sato and K.F. Kobayashi, Laser Cladding of Fe-Cu Based Alloys on Aluminum, *Solid State Phenom.*, 2007, **127**, p 331–336.

13. C.V. Ugarteche et al., Effect of Microstructure on the Thermal Properties of Sintered Iron-Copper Composites, *Mater. Res.*, 2015, **18**, p 1176–1182.

14. E. Dislaki, J. Pokki, S. Pané, J. Sort and E. Pellicer, Fabrication of Sustainable Hydrophobic and Oleophilic Pseudo-Ordered Macroporous Fe–Cu Films with Tunable Composition and Pore Size via Electrodeposition Through Colloidal Templates, *Appl. Mater. Today*, 2018, **12**, p 1–8.

15. Y. Wang, H. Zhao and G. Zhao, Iron-Copper Bimetallic Nanoparticles Embedded within Ordered Mesoporous Carbon as Effective and Stable Heterogeneous Fenton Catalyst for the Degradation of Organic Contaminants, *Appl. Catal. B Environ.*, 2015, **164**, p 396–406.

16. W.L. Wang, Y.H. Wu, L.H. Li, W. Zhai, X.M. Zhang and B. Wei, Liquid-Liquid Phase Separation of Freely Falling Undercooled Ternary Fe-Cu-Sn Alloy, *Sci. Rep.*, 2015, **5**, p 16335.

17. E. Dislaki, J. Sort and E. Pellicer, Parametric Aqueous Electrodeposition Study and Characterization of Fe–Cu Films, *Electrochim. Acta*, 2017, **231**, p 739–748.

18. C.P. Wang, X.J. Liu, I. Ohnuma, R. Kainuma and K. Ishida, Formation of Immiscible Alloy Powders with Egg-Type Microstructure, *Science*, 2002, **297**(5583), p 990–993.

19. T. Prabhakaran et al., Thermally Reduced Soft Magnetic CuFe Nanoparticles for High-Performance Electrical Devices, *IEEE Trans. Magn.*, 2021, **57**, p 2.

20. A. Munitz, A. Venkert, P. Landau, M.J. Kaufman and R. Abbaschian, Microstructure and Phase Selection in Supercooled Copper Alloys Exhibiting Metastable Liquid Miscibility Gaps, *J. Mater. Sci.*, 2012, **47**, p 7955–7970.

21. M. Rabiee, H. Mirzadeh and A. Ataie, Processing of Cu-Fe and Cu-Fe-SiC Nanocomposites by Mechanical Alloying, *Adv. Powder Technol.*, 2017, **28**, p 1882–1887.

22. Y. Chen et al., Microstructure and Strengthening Mechanisms in Cu/Fe Multilayers, *Acta Mater.*, 2012, **60**, p 6312–6321.

23. S. Zhao, S. Zhou, M. Xie, X. Dai, D. Chen and L.C. Zhang, Phase Separation and Enhanced Wear Resistance of Cu88Fe12 Immiscible Coating Prepared by Laser Cladding, *J. Mater. Res. Technol.*, 2019, **8**, p 2001–2010.

24. G.M. Chowla et al., Chemical Precipitation and Properties of Nanocrystalline Fe-Cu Alloy and Composite Powders, *Nanostructured Mater.*, 1992, **1**, p 361–368.

25. X. Zhang, T. Chen, S. Ma, H. Qin and J. Ma, Overcoming the Strength-Ductility Trade-off of an Aluminum Matrix Composite by Novel Core-Shell Structured Reinforcing Particulates, *Compos. Part B*, 2021, **206**, p 108541.

26. W. Wu, B. Guo, Y. Xue, R. Shen, S. Ni and M. Song, Ni-AlxNiy Core-Shell Structured Particle Reinforced Al-based Composites Fabricated by In-situ Powder Metallurgy Technique, *Mater. Chem. Phys.*, 2015, **160**, p 352–358.

27. D. Yadav and R. Bauri, Development of Cu Particles and Cu core-Shell Particles Reinforced Al Composite, *Mater. Sci. Technol.*, 2015, **31**, p 494–500.

28. Y.S. Zhang et al., Core-Shell Structured Titanium-Nitrogen Alloys with High Strength, High Thermal Stability and Good Plasticity, *Sci. Rep.*, 2017, **7**, p 1–8.

29. B. Guo, S. Ni, R. Shen and M. Song, Fabrication of Ti-Al3Ti Core-Shell Structured Particle Reinforced Al Based Composite with Promising Mechanical Properties, *Mater. Sci. Eng. A*, 2015, **639**, p 269–273.

30. Y. Xue, R. Shen, S. Ni, M. Song and D. Xiao, Fabrication, Microstructure and Mechanical Properties of Al-Fe Intermetallic Particle Reinforced Al-based Composites, *J. Alloys Compd.*, 2015, **618**, p 537–544.

31. S.F. Shargh, A. Saadat, A. Najafi, M.R.K. Gharehshiran and G. Khalaj, Investigating the Effect of Post Weld Heat Treatment on Corrosion Properties of Explosive Bonded Interface of AA5083/AA1050/SS 321 Tubes, *Mater Res Express*, 2020, **7**(3), p 036529.

32. M.R.K.G. Shiran, H. Bakhtiari, S.A.A.A. Mousavi, G. Khalaj and S.M. Mirhashemi, Effect of Stand-Off Distance on the Mechanical and Metallurgical Properties of Explosively Bonded 321 Austenitic Stainless Steel-1230 Aluminum Alloy Tubes, *Mater Res*, 2017, **20**, p 291–302.

33. H. Pouraliakbar, G. Khalaj, M.R. Jandaghi, A. Fadaei, M.K. Gharehshiran, S.H. Shim and S.I. Hong, "Three-layered SS321/AA1050/AA5083 Explosive Welds: Effect of PWHT on the Interface Evolution and its Mechanical Strength'', *Int J. Press. Vessel. Pip.*, 2020, **188**, p 104216.

34. S. Ma, X. Zhang, T. Chen and X. Wang, Microstructure-Based Numerical Simulation of the Mechanical Properties and Fracture of a Ti-Al3Ti Core-Shell Structured Particulate Reinforced A356 Composite, *Mater. Des.*, 2020, **191**, p 108685.

35. T. Chen, L. Geng, H. Qin and M. Gao, Core-Shell-Structured Particle Reinforced A356 Matrix Composite Prepared by Powder-Thixoforming: Effect of Reheating Temperature, *Materials (Basel)*, 2018, **11**, p 1–20.

36. T.J. Chen, H. Qin and X.Z. Zhang, Effects of Reheating Duration on the Microstructure and Tensile Properties of In situ Core–Shell-Structured Particle-Reinforced A356 Composites Fabricated via Powder Thixoforming, *J. Mater. Sci.*, 2018, **53**, p 2576–2593.

37. R. Ali, F. Ali, A. Zahoor, H.R. Nawaz, N.U. Haq et al., Effect of Sintering Path on the Microstructural and Mechanical Behavior of Aluminum Matrix Composite Reinforced with Pre-synthesized Al/Cu Core-shell Particles, *J. Alloy. Compd.*, 2021, **889**, p 161531.

38. R. Ali, F. Ali, A. Zahoor, H.R. Nawaz, N.U. Haq et al., Synthesis of Al/Cu Core–Shell Particles Through Optimization of Galvanic Replacement Method in Alkaline Solution, *Int. J. Mater. Res.*, 2021, **112**(6), p 439–447.

39. R. Ali, F. Ali, A. Zahoor, R.N. Shahid, N.U.H. Tariq, S. Ullah and H.B. Awais, A Taguchi Approach to Synthesise Al/Fe Core–Shell Composite Powders Through Electroless Deposition, *Trans IMF*, 2021, **99**(5), p 265–273.

40. G.F. Huang, W.Q. Huang, L.L. Wang, Y. Meng, Z. Xie and B.S. Zou, Electrochemical Study of Electroless Deposition of Fe-P Alloys, *Electrochim. Acta*, 2006, **51**, p 4471–4476.

41. D. Chu, J. Zhang, J. Yao, Y. Han and C. Wu, Cu−Al Interfacial Compounds and Formation Mechanism of Copper Cladding Aluminum Composites, *Trans. Nonferrous Met. Soc. China*, 2017, **27**, p 2521–2528.

42. Y. Guo, G. Liu, H. Jin, Z. Shi and G. Qiao, Intermetallic Phase Formation in Diffusion-Bonded Cu/Al Laminates, *J Mater Sci*, 2011, **46**(8), p 2467–2473.

43. F. Haidara, B. Duployer, D. Mangelinck and M. Record, In-situ Investigation of the Icosahedral Al–Cu–Fe Phase Formation in Thin Films, *J. Alloys Compd.*, 2012, **534**, p 47–51.

44. F. Ali, S. Scudino, M.S. Anwar, R.N. Shahid, V.C. Srivastava, V. Uhlenwinkel and J. Eckert, Al-Based Metal Matrix Composites Reinforced with Al–Cu–Fe Quasicrystalline Particles: Strengthening by Interfacial Reaction, *J Alloys Compd*, 2014, **607**, p 274–279.

45. H. Parsamehr, Y.J. Lu, T.Y. Lin, A.P. Tsai and C.H. Lai, In-Situ Observation of Local Atomic Structure of Al-Cu-Fe Quasicrystal Formation, *Sci. Rep.*, 2019, **9**, p 1245.

46. Y.H. He, Y. Jiang, N.P. Xu, J. Zou, B.Y. Huang, C.T. Liu and P.K. Liaw, Fabrication of Ti–Al Micro/Nanometer-Sized Porous Alloys through the Kirkendall Effect, *Adv Mater*, 2007, **19**(16), p 2102–2106.

47. A. Azarniya, A. Azarniya, A. Abdollah-zadeh, H.R. Madaah Hosseini and S. Ramakrishna, In Situ Hybrid Aluminum Matrix Composites: a Review of Phase Transformations and Mechanical Aspects, *Adv. Eng. Mater.*, 2019, **21**(7), p 1801269.

48. L. Lityńska-Dobrzyńska et al., Characterization of Aluminium Matrix Composites Reinforced by Al-Cu-Fe Quasicrystalline Particles, *J. Alloys Compd.*, 2015, **643**, p S114–S118.

49. F. Ali, S. Scudino, G. Liu, V.C. Srivastava, N.K. Mukhopadhyay, M.S. Khoshkhoo and J. Eckert, Modeling the Strengthening Effect of Al–Cu–Fe Quasicrystalline Particles in Al-Based Metal Matrix Composites, *Journal of Alloys and Compounds*, 2012, **536**, p S130–S133.

50. S. Scudino, G. Liu, K.G. Prashanth, B. Bartusch, K.B. Surreddi, B.S. Murty and J. Eckert, Mechanical Properties of Al-Based Metal Matrix Composites Reinforced with Zr-Based Glassy Particles Produced by Powder Metallurgy, *Acta Mater.*, 2009, **57**, p 2029–2039.